Journal of Solid Mechanics Vol. 13, No. 4 (2021) pp. 485-502
DOI: 10.22034/jsm.2020.1913430.1653

Large Deformation Hermitian Finite Element Coupled Thermoelasticity Analysis of Wave Propagation and Reflection in a Finite Domain

M. Mirparizi [1], M. Shariyat [2,*], A.R. Fotuhi [1]

[1] *Department of Mechanical Engineering, Yazd University, Yazd, Iran*
[2] *Faculty of Mechanical Engineering, K.N. Toosi University of Technology, Tehran, Iran*

Received 1 August 2021; accepted 7 October 2021

ABSTRACT

In the present paper, a finite element nonlinear coupled thermoelasticity formulation is presented for analysis of the wave propagation, reflection, and mixing phenomena in the finite length isotropic solids. The governing equations are derived based on the second Piola-Kirchhoff stress and the full form of Green's strain-displacement tensors to account for the large deformations and finite strains. In contrast to the available researches, the assumption of very small temperature changes compared to the reference temperature is released in the present research. Galerkin's method, a weak formulation, and cubic elements are employed to obtain the time-dependent non-linear finite element governing equations. The proposed solution procedure to the resulting highly nonlinear and time-dependent governing equations employs an updating algorithm and Newmark's numerical time integration method. The wave propagation and reflection phenomena are investigated for both the mechanical and thermal shocks and time variations of distributions of the resulting displacements, temperature rises, and stresses are illustrated graphically and discussed comprehensively. Furthermore, the effects of the non-linear terms are discussed comprehensively. Results reveal that in the non-linear analysis, no fixed speed of wave propagation can be defined.

Keywords : Coupled thermoelasticity; Finite strain; Thermal shock; Surface traction; Wave propagation and reflection.

1 INTRODUCTION

DUE to the probable occurrence of catastrophic failures, determination of the transient structural responses in time instants immediately after exposure to a thermoelastic shock is an important issue in many engineering applications, such as mechanical, electrical power, nuclear, chemical, and aerospace engineering. Publication of the first books on thermal stresses, e.g., by Melan and Parkus [1] and Nowacki [2-4] was the most important stage in the progress of the thermoelasticity. Danilovskaya [5] pioneered the first research on the one-dimensional dynamic

*Corresponding author.
E-mail address: shariyat@kntu.ac.ir (M. Shariyat).

thermoelasticity problem of thermal stresses in a half-space. The main studies in this field have considered the occurrence of large displacements and small strains. In this regard, Manoach and Ribeiro [6] studied nonlinear vibrations of thick beams under the combined action of mechanical and thermal loads. They also investigated the influence of the time duration and amplitude of the thermal loading on time histories of the responses of the structure. Vujošević and Lubarda [7] derived the constitutive formulation of the finite-strain thermoelasticity by multiplicative decomposition of the deformation gradient. Abo-El-Nour et al. [8] presented an analytical solution for nonlinear thermoelasticity problems with special boundary conditions. Slemrod [9] derived the governing equations of the nonlinear thermoelasticity and provided an appropriate evolution equation but neglected the infinitesimal strain expressions and used the method of Lions-Faedo-Galerkin. Rawy et al. [10] proposed a numerical solution for the nonlinear, one-dimensional problem of thermoelasticity. Sweilam [11] employed the variational iteration and Adomian's decomposition methods to numerically solve the governing equations of the harmonic wave generation in a one-dimensional non-linear elastic half-space. Rogovoi and Stolbova [12] obtained the equation of state of the finite-strain coupled thermoelasticity, using a variational approach, to construct the constitutive relations for complex media under the assumption of the closeness of the intermediate and current configurations. Wave propagation in initially-stressed elastic rods was investigated by Kocakaplan and Tassoulas [13]. Marzani et al. [14] proposed a finite element solution to analyze the wave propagation in axisymmetric waveguides [15].

The foregoing brief review reveals that the majority of the available researches on the one-dimensional coupled thermoelasticity have not treated the wave propagation and especially, reflection; as the majority of them have studied the thermoelasticity problem for the half-space, rather than a finite domain. Furthermore, some of the 1D thermoelasticity models that have studied the coupled thermoelasticity problem in a finite domain, have either used linear strain-displacement expressions [16-18] or used linear elements (which results in jumps in the stress components at the mutual nodes and edges of the elements). In the lights of these issues, novelties of the present research may be summarized as:

(1) Presenting a finite element coupled thermoelasticity formulation that may be used for large deformations as well,
(2) Investigation of both wave propagation and wave reflection phenomena,
(3) Incorporation of the traction boundary condition through a novel procedure,
(4) Proposing a solution algorithm for solving the resulting highly nonlinear coupled governing equations,
(5) Presenting a new idea in the development of the weak formulation.
(6) Using cubic elements to obtain more accurate results. Employing the common linear elements usually lead to less accurate and sometimes, erroneous results.

2 THE NONLINEAR COUPLED GOVERNING EQUATIONS OF THERMOELASTICITY

2.1 The energy balance and motion equations

Let us investigate the problem of thermoelastic wave propagation, reflection, and interference within the finite-length medium shown in Fig. 1. The limited available researches on non-linear thermoelasticity have focused on half-spaces. Therefore, no wave reflection or thermal/stress wave mixing have been noticed in their findings. Moreover, since their goal was presenting semi-analytical solutions, the results were generally presented for special forms of the excitations that seldom occur. No limitations have been considered for the thermoelastic loads in the present analysis. When using the full form of the strain-displacement expressions or expecting the occurrence of large deformations, the nonlinear time-dependent governing equations of motion and the heat conduction equation of each material element may respectively be expressed as [9, 19- 21]:

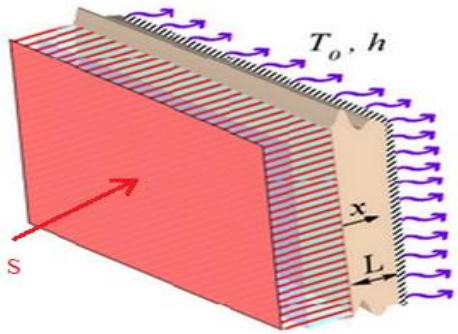

Fig.1
Geometric parameters and the imposed thermomechanical loads of the considered finite length solid.

$$Div\{[I+\nabla u(X,t)]s(X,t)\}+\rho_0 b(X,t)=\rho_0\frac{\partial^2 u}{\partial t^2}(X,t) \tag{1}$$

$$\rho_0\frac{\partial e}{\partial t}(X,t)=tr\left(s^T(X,t)\frac{\partial E}{\partial t}(X,t)\right)-Divq(X,t)+\rho_0 r(X,t) \tag{2}$$

where *u, t, s*, ρ_0, *b, e, r*, and *E* are, respectively, the longitudinal displacement, time, second Piola-Kirchhoff stress tensor, reference mass density, body force, intrinsic energy, heat generation per unit mass, and Green's strain tensor with the following definition:

$$E=\frac{1}{2}\left[\nabla u+(\nabla u)^T+(\nabla u)^T\nabla u\right] \tag{3}$$

In Eq.(2), it is assumed that the material properties are temperature-independent, within the considered temperature rise. For a one-dimensional thermoelasticity, the instantaneous coordinates of each particle (x_i) may be related to its initial coordinates (X_i) according to the following transformation equation:

$$x_1=x_1(X_1,t),\qquad x_2=X_2,\qquad x_3=X_3 \tag{4}$$

Therefore, the displacement, deformation gradient, strain–displacement expression, and second Piola-Kirchhoff stress can, respectively, be determined from:

$$U(X_1,t)=x_1(X_1,t)-X_1 \tag{5}$$

$$F=\begin{bmatrix}1+\dfrac{\partial U}{\partial X_1} & 0 & 0\\ 0 & 1 & 0\\ 0 & 0 & 1\end{bmatrix} \tag{6}$$

$$E=\begin{bmatrix}\left(1+\dfrac{1}{2}\dfrac{\partial U}{\partial X_1}\right)\dfrac{\partial U}{\partial X_1} & 0 & 0\\ 0 & 0 & 0\\ 0 & 0 & 0\end{bmatrix} \tag{7}$$

$$s=\begin{bmatrix}s_{11} & 0 & 0\\ 0 & 0 & 0\\ 0 & 0 & 0\end{bmatrix} \tag{8}$$

where *U* is the displacement component. Since the considered problem is a 1*D* one, dimensions of the medium in directions perpendicular to the wave propagation directions (i.e., in X_2 and X_3 directions) are chosen to be infinity. For the sake of simplicity in writing, one may drop the subscript 1 from the parameters, e.g.;

$$X_1\to X,\qquad s_{11}\to s \tag{9}$$

Then, the second Piola-Kirchhoff stress may be obtained in the reference configuration as [21]:

$$s=(\lambda+2\mu)E-\beta(T-T_0) \tag{10}$$

where λ and μ are Lame constants of the isotropic elastic continuum, $\beta = \alpha_T (3\lambda + 2\mu)$, and α_T is the thermal expansion coefficient. Substituting Eqs. (3) to (10) into Eq. (1) and noting that $T = T_0\left(1+\frac{\theta}{T_0}\right)$, leads to the following nonlinear equation of motion:

$$\rho_0 \frac{\partial^2 U}{\partial t^2} - (\lambda+2\mu)\frac{\partial^2 U}{\partial X^2} - 3(\lambda+2\mu)\frac{\partial^2 U}{\partial X^2}\frac{\partial U}{\partial X} - \frac{3}{2}(\lambda+2\mu)\frac{\partial^2 U}{\partial X^2}\left(\frac{\partial U}{\partial X}\right)^2 + \alpha_T (3\lambda+2\mu)\frac{\partial U}{\partial X}\frac{\partial \theta}{\partial X} + \alpha_T (3\lambda+2\mu)\frac{\partial \theta}{\partial X} + \alpha_T (3\lambda+2\mu)\frac{\partial^2 U}{\partial X^2}\theta - \rho_0 b = 0 \tag{11}$$

It may be reminded that displacements of the medium are not restricted in X_2 and X_3 directions, as Eq. (8) implies. According to Fourier's law, the heat flux per current area may be related to the temperature gradient as:

$$q = -k\frac{\partial T}{\partial X} \tag{12}$$

So that, combining the second law of thermodynamics and Fourier's law leads to [20,21]:

$$c_\varepsilon \rho_0 \left(\frac{\partial T}{\partial t}\right) = k\left(\frac{\partial^2 T}{\partial X^2}\right) - T_0\beta\left(1+\frac{T-T_0}{T_0}\right)\frac{\partial E}{\partial t} + \rho_0 r \tag{13}$$

Substituting Eq. (3) into Eq. (13) gives the nonlinear energy balance equation in the following form:

$$c_\varepsilon \rho_0 \frac{\partial \theta}{\partial t} + \beta(\theta+T_0)\left(\frac{\partial^2 U}{\partial X\,\partial t} + \frac{\partial^2 U}{\partial X\,\partial t}\frac{\partial U}{\partial X}\right) - k\frac{\partial^2 \theta}{\partial X^2} - \rho_0 r = 0 \tag{14}$$

where c_ε is the specific heat capacity and k is the thermal conductivity coefficient.

2.2 The geometric and boundary conditions

Fig. 1 shows geometric parameters as well as the imposed thermomechanical loads of the finite length solid. The backplane of the body is fixed. Therefore, the wave reflection happens with a higher intensity. The body may be subjected to a shock in the form of either surface traction (τ) or a temperature rise ($\theta = T - T_0$) on one side and a convection heat transfer at the other side of the medium.

Since the thermoelastic behaviors resulting from the mechanical impulse loading differ from those caused by thermal shocks, the resulting thermoelastic stresses, and displacements, as well as the wave propagation and reflection phenomena, are considered for the following two distinct loading conditions:

i) Impulsive compressive traction that is imposed for a very time duration, on the beginning plane of the body (Fig. 1) while both the front and back planes of the body are exposed to a convection heat transfer with the ambient.

$$\begin{cases} \sigma(0,t) = \begin{cases} \tau_0 & t_1 \le t \le t_2 \\ 0 & t > t_2 \end{cases} \\ U(L,t) = 0 \\ -k\left.\frac{\partial \theta}{\partial X}\right|_{X=0} + h(\theta)|_{X=0} = 0 \\ k\left.\frac{\partial \theta}{\partial X}\right|_{X=L} + h(\theta)|_{X=L} = 0 \end{cases} \tag{15}$$

where σ is the Cauchy stress.

ii) The front plane of the domain is subjected to a temperature rise shock with a high rate of decay while the backplane is under a convection heat transfer:

$$\begin{cases} \sigma(0,t)=0 \\ U(L,t)=0 \\ \theta(0,t)=\theta_0\times(10^5 t)\times e^{-2\times10^5 t} \\ k\left.\dfrac{\partial\theta}{\partial X}\right|_{X=L}+h(\theta)\big|_{X=L}=0 \end{cases} \tag{16}$$

For both cases, it is assumed that all particles of the domain are initially at rest and experience the ambient temperature; so that, the associated initial conditions are:

$$\begin{cases} U(X,0)=\dot{U}(X,0)=0 \\ T(X,0)=T_0 \rightarrow \theta(X,0)=0 \end{cases} \tag{17}$$

Although the full Green's non-linear strain-displacement expressions are employed for both types of examples, from a practical point of view, large deformations in a one-dimensional domain may occur due to the first type of problems. Because large deformations in the second type problem may take place when a significantly high-temperature rise is employed. In such a case, either a local melting or a high temperature-rise that requires considering the temperature-dependency of the material properties may happen.

3 THE FINITE ELEMENT FORM OF THE GOVERNING EQUATIONS AND THE BOUNDARY CONDITIONS

The first-order elements generally lead to erroneous or inaccurate results in structural analyses, unless a huge number of elements (*h*-method refinement) is used. It has been proven that the highest accuracy is obtained when the order of the shape functions is larger than that of the order of the weak form of the governing equations by one [22]. Since, as explained later, the order of the weak forms of the governing system of Eqs. (11) and (14) is not less than 2, cubic elements are employed in the present research. Many researchers have already proven that using high-order elements (*p*-method refinement) leads to significantly reducing the computations [17,22-26]. In this regard, spatial variations of the domain degrees of freedom, i.e., main variables of Eqs. (11) and (14) can be traced by the adopted cubic shape functions:

$$U(x,t)=\sum_{j=1}^{n}u_j^e(t)N_j^e(x) \qquad \theta(x,t)=\sum_{j=1}^{n}\theta_j^e(t)N_j^e(x) \tag{18}$$

where u_j^e,θ_j^e are the nodal vectors of the displacement component and the temperature rise and $N_j^e(x)$ are the third-order shape functions that may be expressed in terms of local coordinate as [22]:

$$\begin{aligned} N_1^e(x)&=(1-\frac{3\bar{X}}{l_e})(1-\frac{3\bar{X}}{2l_e})(1-\frac{\bar{X}}{l_e}) \\ N_2^e(x)&=9\frac{\bar{X}}{l_e}\left(1-\frac{3\bar{X}}{2l_e}\right)\left(1-\frac{\bar{X}}{l_e}\right) \\ N_3^e(x)&=-\frac{9}{2}\frac{\bar{X}}{l_e}\left(1-\frac{3\bar{X}}{l_e}\right)\left(1-\frac{\bar{X}}{l_e}\right) \\ N_4^e(x)&=\frac{\bar{X}}{l_e}\left(1-\frac{3\bar{X}}{l_e}\right)\left(1-\frac{3\bar{X}}{2l_e}\right) \end{aligned} \tag{19}$$

where $l_e = \bar{X}_2^{(e)} - \bar{X}_1^{(e)}$ and $\bar{X}_1^{(e)}$ and $\bar{X}_2^{(e)}$ are coordinates of the beginning and end grid points of the element. The augmented vector of the degrees of freedom can be established as:

$$\boldsymbol{\varphi} = \begin{Bmatrix} u \\ \theta \end{Bmatrix} = \begin{bmatrix} N_1^e & N_2^e & N_3^e & N_4^e & 0 & 0 & 0 & 0 \\ 0 & 0 & 0 & 0 & N_1^e & N_2^e & N_3^e & N_4^e \end{bmatrix} \begin{Bmatrix} \boldsymbol{u}^{(e)} \\ \boldsymbol{\theta}^{(e)} \end{Bmatrix} = \begin{bmatrix} \boldsymbol{N} & \mathbf{0} \\ \mathbf{0} & \boldsymbol{N} \end{bmatrix} \begin{Bmatrix} \boldsymbol{u}^{(e)} \\ \boldsymbol{\theta}^{(e)} \end{Bmatrix} = \hat{\boldsymbol{\mathcal{N}}} \boldsymbol{\Phi} \tag{20}$$

Therefore, Galerkin's form of the governing differential Eqs. (11) and (14) has the following form:

$$\int_{\bar{X}_1^{(e)}}^{\bar{X}_2^{(e)}} \hat{\boldsymbol{\mathcal{N}}}^T \begin{Bmatrix} \mathcal{R}_1 \\ \mathcal{R}_2 \end{Bmatrix} d\bar{X} = \mathbf{0} \tag{21}$$

where $\mathcal{R}_1 = 0$ and $\mathcal{R}_2 = 0$ correspond to Eqs. (11) and (14), respectively. The weak form of the weighted residual Eq. (21) may be represented by:

$$\boldsymbol{\mathcal{M}} \ddot{\boldsymbol{\Phi}} + [\boldsymbol{\mathcal{C}}(\boldsymbol{\Phi})] \dot{\boldsymbol{\Phi}} + [\boldsymbol{\mathcal{K}}(\boldsymbol{\Phi})] \boldsymbol{\Phi} = \mathrm{F} + \boldsymbol{R} \tag{22}$$

In this regard, one may reduce the order of as much as terms possible. This hint leads to resulting terms with higher-order dependency on $\bar{X}$, for an identical order of the shape functions and in turn, enables computing the integrals more accurately and incorporates the thermal boundary conditions more adequately. In Eq. (22):

$$\boldsymbol{\mathcal{M}} = \begin{bmatrix} \mathbf{M}_{11} & \mathbf{M}_{12} \\ \mathbf{M}_{21} & \mathbf{M}_{22} \end{bmatrix}, \qquad \mathbf{M}_{11} = \rho_0 \int_{\bar{X}_1^{(e)}}^{\bar{X}_2^{(e)}} \boldsymbol{N}^T \boldsymbol{N} \, dX \ , \qquad \mathbf{M}_{12} = \mathbf{M}_{21} = \mathbf{M}_{22} = 0 \tag{23}$$

$$\begin{aligned} &\boldsymbol{\mathcal{C}} = \begin{bmatrix} \mathbf{C}_{11} & \mathbf{C}_{12} \\ \mathbf{C}_{21} & \mathbf{C}_{22} \end{bmatrix}, \quad \mathbf{C}_{11} = \mathbf{C}_{12} = 0, \qquad \mathbf{C}_{21} = \beta \int_{\bar{X}_1^{(e)}}^{\bar{X}_2^{(e)}} (\theta + T_0) \left(1 + \frac{\partial U}{\partial X} \right) \boldsymbol{N}^T \boldsymbol{N}_{,x} dX \ , \\ &\mathbf{C}_{22} = c_\varepsilon \rho_0 \int_{\bar{X}_1^{(e)}}^{\bar{X}_2^{(e)}} \boldsymbol{N}^T \boldsymbol{N} \, dX \end{aligned} \tag{24}$$

$$\begin{aligned} &[\boldsymbol{\mathcal{K}}(\boldsymbol{\Phi})] = \begin{bmatrix} \mathbf{K}_{11} & \mathbf{K}_{12} \\ \mathbf{K}_{21} & \mathbf{K}_{22} \end{bmatrix} \\ &\mathbf{K}_{11} = -3(\lambda + 2\mu) \left[\int_{\bar{X}_1^{(e)}}^{\bar{X}_2^{(e)}} \boldsymbol{N}^T \left[\frac{\partial U}{\partial X} + \frac{1}{2} \left(\frac{\partial U}{\partial X} \right)^2 \right] \boldsymbol{N}_{,xx} dX \right] dX \\ &+ (\lambda + 2\mu) \int_{\bar{X}_1^{(e)}}^{\bar{X}_2^{(e)}} \boldsymbol{N}_{,x}^T \boldsymbol{N}_{,x} dX - \alpha_T (3\lambda + 2\mu) \int_{\bar{X}_1^{(e)}}^{\bar{X}_2^{(e)}} (\theta \boldsymbol{N}_{,x}^T + \theta_{,x} \boldsymbol{N}^T) \boldsymbol{N}_{,x} dX \\ &- \left[[(\lambda + 2\mu) - \alpha_T (3\lambda + 2\mu) \theta] \boldsymbol{N}^T \boldsymbol{N}_{,x} \right|_{\bar{X}_1^{(e)}}^{\bar{X}_2^{(e)}} \\ &\mathbf{K}_{12} = \alpha_T (3\lambda + 2\mu) \int_{\bar{X}_1^{(e)}}^{\bar{X}_2^{(e)}} \left(1 + \frac{\partial U}{\partial X} \right) \boldsymbol{N}^T \boldsymbol{N}_{,x} dX \\ &\mathbf{K}_{21} = 0, \qquad \mathbf{K}_{22} = k \int_{\bar{X}_1^{(e)}}^{\bar{X}_2^{(e)}} \boldsymbol{N}_{,x}^T \boldsymbol{N}_{,x} dX \end{aligned} \tag{25}$$

$$\mathrm{F} = \begin{Bmatrix} \mathbf{f} \\ \mathcal{Q} \end{Bmatrix}, \quad \mathbf{f} = \rho_0 \int_{\bar{X}_1^{(e)}}^{\bar{X}_2^{(e)}} \boldsymbol{N}^T b \, dX \ , \quad \mathcal{Q} = k \boldsymbol{N}^T \left. \frac{\partial \theta}{\partial x} \right|_{\bar{X}_1^{(e)}}^{\bar{X}_2^{(e)}} = -q \boldsymbol{N}^T \Big|_{\bar{X}_1^{(e)}}^{\bar{X}_2^{(e)}}, \quad R = \begin{Bmatrix} \mathbf{0} \\ \rho_0 \int_{\bar{X}_1^{(e)}}^{\bar{X}_2^{(e)}} \boldsymbol{N}^T r dX \end{Bmatrix} \tag{26}$$

It is worth mentioning that the order of the weighted third and fourth terms of Eq. (11) does not lead to weak formulations, e.g.;

$$
\begin{aligned}
&3(\lambda+2\mu)\int_{\bar{X}_1^{(e)}}^{\bar{X}_2^{(e)}} \boldsymbol{N}^T \frac{\partial^2 U}{\partial X^2}\frac{\partial U}{\partial X}dX \\
&= 3(\lambda+2\mu)\left[\boldsymbol{N}^T\left(\frac{\partial U}{\partial X}\right)^2\Bigg|_{\bar{X}_1^{(e)}}^{\bar{X}_2^{(e)}} - \int_{\bar{X}_1^{(e)}}^{\bar{X}_2^{(e)}}\left(\boldsymbol{N}_{,x}^T\frac{\partial U}{\partial X}+\boldsymbol{N}^T\frac{\partial^2 U}{\partial X^2}\right)\boldsymbol{N}_{,x}\boldsymbol{u}^{(e)}dX\right]
\end{aligned}
\tag{27}
$$

For this reason, these terms are not manipulated in Eq. (25). This is why cubic rather than quadratic elements are used. The traction boundary condition (15) can be assembled with Eq. (22), after interpreting it in the following finite element form:

$$
\begin{aligned}
s(0,t)=\tau_0 &= \left[(\lambda+2\mu)\left(1+\frac{1}{2}\frac{\partial U}{\partial X}\right)\mathbf{N}_{,x}\mathbf{u}^{(1)}-\beta\mathbf{N}\theta^{(1)}\right]_{\bar{X}=0} \\
&= \left[(\lambda+2\mu)\left(1+\frac{1}{2}\frac{\partial U}{\partial X}\right)\mathbf{N}_{,x}\Big|_{\bar{X}=0} \quad -\beta\mathbf{N}\Big|_{\bar{X}=0}\right]\boldsymbol{\Phi}^{(1)}
\end{aligned}
\tag{28}
$$

The $\theta, \frac{\partial U}{\partial X}$, and $\frac{\partial^2 U}{\partial X^2}$ expressions appeared in Eqs. (22) to (26) can also be substituted by appropriate finite element expressions.

4 THE SOLUTION PROCEDURE OF THE NONLINEAR COUPLED SYSTEM OF EQUATIONS

In the foregoing section, the nonlinear system of governing Eqs. (11) and (14) was reduced to a nonlinear system of ordinary finite element Eqs. (22) in time. The boundary conditions, such as Eq. (28) have to be incorporated before solving the resulting system of equation in the time domain.

The solution of the governing equations in the time domain requires the discretization of the time domain into time steps that are much smaller than the period time associated with the fundamental natural frequency of the system (about its current state). It is evident the oscillations of the temperature require remarkably larger times. The adopted time step is $\Delta t = 10^{-5} s$. Employing Newmark's numerical time integration procedure [22] for the *ith* time step, one may write:

$$
\ddot{\boldsymbol{\Phi}}_{i+1} = a_3(\boldsymbol{\Phi}_{i+1}-\boldsymbol{\Phi}_i)-a_4\dot{\boldsymbol{\Phi}}_i - a_5\ddot{\boldsymbol{\Phi}}_i \tag{29}
$$

$$
\dot{\boldsymbol{\Phi}}_{i+1} = \dot{\boldsymbol{\Phi}}_i + a_2\ddot{\boldsymbol{\Phi}}_i + a_1\ddot{\boldsymbol{\Phi}}_{i+1} \tag{30}
$$

Eqs. (29) and (30) may reduce the resulting system of equations to a nonlinear system of algebraic equations of the following form:

$$
\left[\mathcal{K}^*(\boldsymbol{\Phi})\right]_{i+1}\boldsymbol{\Phi} = \mathbf{F}_{i+1}^* \tag{31}
$$

where:

$$
\begin{aligned}
&\left[\mathcal{K}^*\right]_{i+1} = \left[\mathcal{K}^*\right]_i + a_3\boldsymbol{\mathcal{M}}_{i+1} - a_1a_3\boldsymbol{\mathcal{C}}_{i+1} \\
&\mathbf{F}_{i+1}^* = \mathbf{F}_i^* + \boldsymbol{\mathcal{M}}_{i+1}(a_3\boldsymbol{\Phi}_i + a_4\dot{\boldsymbol{\Phi}}_i + a_5\ddot{\boldsymbol{\Phi}}_i) - \\
&\boldsymbol{\mathcal{C}}_{i+1}\left[(a_2 - a_1a_4 - a_1a_5)\ddot{\boldsymbol{\Phi}}_i + \dot{\boldsymbol{\Phi}}_i - a_1a_3\boldsymbol{\Phi}_i\right] + \boldsymbol{R}
\end{aligned}
\tag{32}
$$

$$
a_1 = \alpha\Delta t, \qquad a_2 = (1-\alpha)\Delta t, \qquad a_3 = \frac{2}{\gamma(\Delta t)^2}, \quad a_4 = a_3\Delta t, \qquad a_5 = \frac{1}{\gamma}-1 \tag{33}
$$

where Δt is the time increment. The choice of α and γ parameters affects the stability and accuracy of the solution. According to the second-order Runge-Kutta method: $\alpha = \frac{1}{2}, \gamma = \frac{1}{2}$. For the first time step, the initial conditions $\boldsymbol{\Phi}_0$ and $\dot{\boldsymbol{\Phi}}_0$ are assumed to be zero and the acceleration vector is computed from Eq. (22) to be:

$$\ddot{\boldsymbol{\Phi}}_0 = \boldsymbol{\mathcal{M}}^{-1}(\mathbf{F} + \boldsymbol{R})_0 \tag{34}$$

The resulting element stiffness matrix is still dependent on $\boldsymbol{\Phi}_{i+1}$; so that, the system of Eq. (31) is nonlinear and asymmetric. In each time step, Picard's iterative solution procedure may be used in this regard [27-29]:

$$\boldsymbol{\Phi}_{i+1}^{1} = \boldsymbol{\Phi}_i \quad , \qquad \boldsymbol{\Phi}_{i+1}^{m+1} = \left[\boldsymbol{\mathcal{K}}^*(\boldsymbol{\Phi}_{i+1}^{m})\right]_{i+1}^{-1} \mathbf{F}_{i+1}^{*} \; ; \; m \geq 1 \tag{35}$$

where m is the iteration counter. The iterative solution is continued until convergence is achieved. The following criterion is chosen to check the convergence:

$$\frac{\left\| \boldsymbol{\Phi}_{i+1}^{m+1} - \boldsymbol{\Phi}_{i+1}^{m} \right\|}{\left\| \boldsymbol{\Phi}_{i+1}^{m+1} \right\|} << \varepsilon \tag{36}$$

where ε is a negligible number. After each iteration, a modified $\boldsymbol{\Phi}$ is obtained which in turn can be employed to update the stiffness of the entire domain to be used in the next iteration.

5 NUMERICAL RESULTS AND DISCUSSIONS

5.1 Validation of the results

To verify the results, a linear problem of half-space previously studied by Youssef and Al-Lehaibi [30] is reexamined. The boundary plane at x=0 is traction free and subjected to a step temperature rise $\theta(0,t) = \varphi_0 H(t)$ where $H(t)$ is Heaviside's unit step function ($T_0 = 293\ K$). The medium is fabricated from copper with the following material properties:

$$K = 386\ N/Ks, \quad a_T = 1.78\times10^{-5} K^{-1}, \quad \mathrm{c}_\varepsilon = 383.1\ m^2/K, \quad \rho = 8954\ kg/m^3,$$
$$\mu = 3.86\times10^{10} N/m^2, \quad \lambda = 7.76\times10^{10} N/m^2$$

Since a linear thermoelasticity approach was adopted by Youssef and Lehaibi, using an analytical solution and Laplace transform and state-space techniques were available [31,32]. Youssef and Al-Lehaibi presented their results using the theory of two-temperature generalized. The following dimensionless terms were introduced to obtain the results:

$$\theta' = \frac{T - T_0}{T_0}, \quad \sigma' = \frac{\sigma}{\mu}, \quad u' = \sqrt{\left(\frac{\lambda+2\mu}{\rho}\right)}\frac{u}{k}, \quad t' = \left(\frac{\lambda+2\mu}{\rho}\right)\frac{t}{k}, \quad x' = \sqrt{\left(\frac{\lambda+2\mu}{\rho}\right)}\frac{x}{k} \tag{37}$$

The results are obtained for $t = 0.2(s)$ and $,\varphi_0 = 1$. The resulting time histories of the dimensionless temperature-rise and stress are compared with those of [30] at x=0.2 section in Figs. 2 and 3. As may readily deduced from Figs. 2 and 3 that the temperature and stress of the considered section increase with time (wave propagation) and the temperature converges toward a certain amount, as t' tends to infinity. Due to the thermoelastic coupling, these oscillations affect the temperature rise within the body as well. On the other hand, the numerical Laplace inversion equation uses two floating parameters that their optimum values not only vary from a problem to another but also within the same time history and thus, cannot be assigned accurately [31,32]. Moreover, the number of engaged vibration modes depends on the number of summation terms. Generally, the present

numerical time integration can trace the instantaneous fluctuations. Hence, in addition to the fact that the present results show a good concordance with those obtained by Youssef and Lehaibi, they give a stronger physical sense.

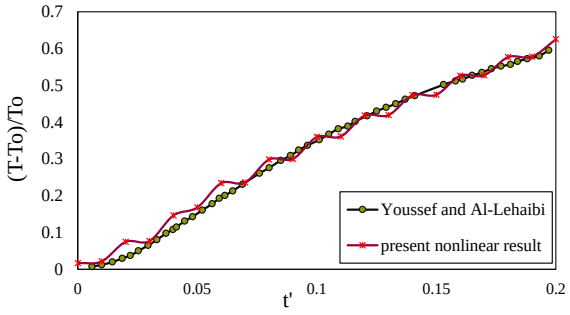

Fig.2
Comparison between time variations of the temperature predicted by the present research and those of the semi-analytical model of Youssef and Al-Lehaibi, at (x=0.2).

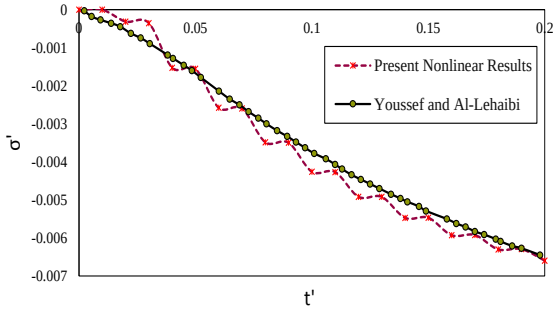

Fig.3
Comparison between time variations of the stress predicted by the present research and those of the semi-analytical model of Youssef and Al-Lehaibi, at (x=0.2).

The longitudinal distributions of stresses and displacements are presented in Figs. 4 and 5 and compared with the predicted results of Youssef and Lehaibi. Fig. 4 illustrates that the displacements grow with time whereas Fig. 5 reveals that the stress wavefront has reached the x=0.09 plane; so that point the behind sections are pulled to compress the front sections, as the wave travels across the domain. The analytical results of Youssef indicate a jump in the stress distribution at the instantaneous location of the stress wavefront. It is evident that all the discretization techniques, such as the finite element, boundary element, differential quadrature, and meshless methods cannot show the local jumps and discontinuities in the quantities and regard them as residual errors that must be distributed over the whole domain [33,34].

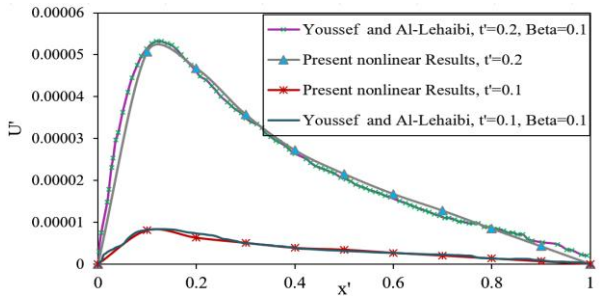

Fig.4
Comparison between displacement distributions predicted by the present research and those of the semi-analytical model of Youssef and Al-Lehaibi, (t'=0.1 and t'=0.2).

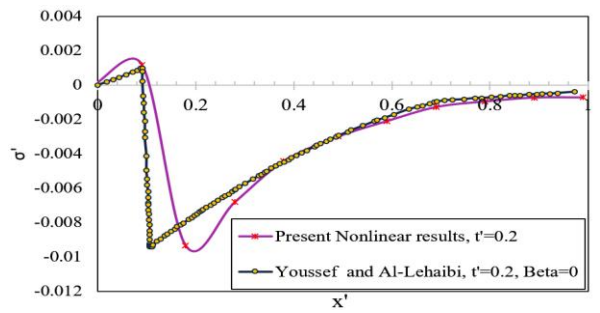

Fig.5
Comparison between stress distributions predicted by the present research and those of the semi-analytical model of Youssef and Al-Lehaibi, (t'=0.1 and t'=0.2).

As another validation example, the outcomes are compared with those of the finite element solution given by Ting and Chen [35] that predicted a solution for anisotropic elastic medium subjected to a convection heat transfer with this boundary conditions:

$$\begin{cases} T(0,t) = T_0 & ; \quad (t < 0) \\ k \left. \dfrac{\partial T}{\partial X} \right|_{x=0} = h(T|_{x=0} - T_\infty) ; & \quad (t \geq 0) \end{cases} \tag{38}$$

These non-dimensional parameters are employed to express the obtained results:

$$x' = \frac{ax}{d}, \quad t' = \frac{a^2 t}{d}, \quad \sigma' = \frac{\sigma_x}{T - T_0}, \quad \theta' = \frac{T - T_0}{T_0} \quad (d = \frac{k}{C}, a = \sqrt{\frac{\lambda + 2\mu}{\rho}}) \tag{39}$$

Time history of the temperature rise and stress are demonstrated in Figs. 6 and 7, for x'=1. Although the results show a relatively good agreement, since Ting and Chen [35] used linear shape functions, their results, especially the stress results are not as accurate as the present results that have been extracted using cubic shape functions. For this reason, the results of the solution presented in this research, are more similar to the exact results (Lee and Sim [36]), as Fig. 7 confirms.

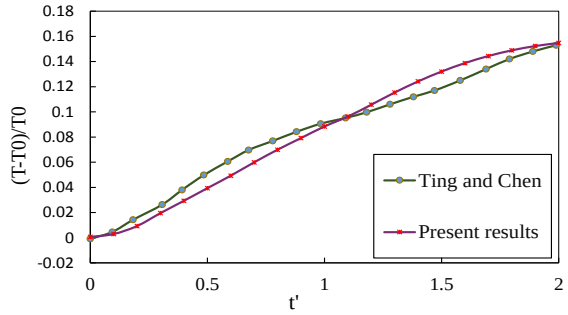

Fig.6
Comparison between the temperature-rise results of the first-order [35] and third-order (present) finite element models (x'=0.1).

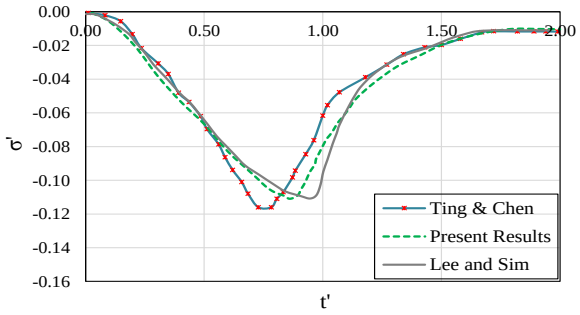

Fig.7
Comparison between the stress results of the first-order [35] and third-order (present) fine element models (x'=0.1).

5.2 Investigation of wave propagation/reflection and mixing phenomena in a finite length domain
5.2.1 Anisotropic elastic solid exposed to a traction shock and convection

Boundary conditions of the domain have appeared in Eq. (15). The material properties of the selected stainless-steel are listed in Table 1.

Table 1
Material properties of stainless steel [37].

$T_0 = T_\infty$	$h(w/m^2K)$	$E(N/m^2)$	$c_\varepsilon(j/kgK)$	$\rho(kg/m^3)$	$\alpha(K^{-1})$	$k(w/mK)$
25^0C	100	189.5×10^9	500	7700	12×10^{-6}	16.5

The other required parameters are introduced in the following:

$$L = 2m,\quad \Delta t = 10^{-5}s,\quad \tau_0 = 10^6 Pa,\quad t_1 = 0,\quad t_2 = 3\times\Delta t(s),\quad \theta_0 = 100^{\circ}C$$

The domain is discretized into 100 cubic elements. The time histories of the stress observed in different sections as the stress wave travels through the domain because of the applied traction shock are demonstrated in Fig. 8. As may be observed, in the early times, stresses are zero in some sections. This phenomenon confirms the stress wave propagation with a speed approximately equal to $v = \sqrt{(\lambda+2\mu)/\rho} \simeq 5238(m/s)$. The stress wave has arrived at the end plane of the solid $(X \simeq 2(m))$, approximately after $t \simeq 3.8\times10^{-1}(ms)$. After this time, by changing the stress sign, wave reflection starts. Fig. 9 shows the longitudinal distribution of the stress, for various time instants. At the shock time duration, only regions that are located in the neighborhood of the front plane have sensed the imposed compressive traction. Followed by the pressure shock elimination, the wave travels in the medium until $t \simeq 3.8\times10^{-1}(ms)$. The reversion of the wave propagation (reflection) begins after $t \simeq 4\times10^{-1}(ms)$, (Fig.9 (c)), which induces tensile stresses after a transition situation. Fig. 10 demonstrates the time histories of the non-dimensional displacement observed at various planes of the domain. Before $t \simeq 0.38(ms)$, all sections, travel in the positive axis (Fig. 10). Followed by that time, wave reflection begins, and opposite motions will begin as well. Moreover, the wave propagation phenomenon in the medium due to the mechanical shock may be explored by studying the displacement distribution at successive time instants.

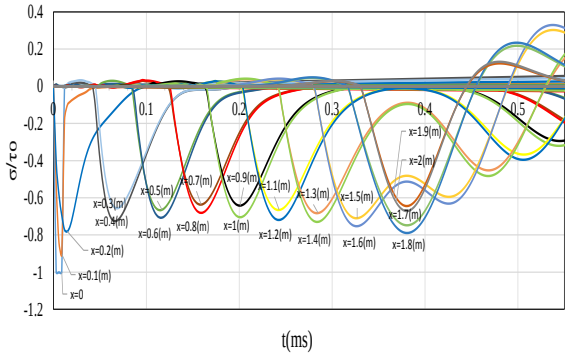

Fig.8
Stress time histories observed at different sections of the medium. after exposure to the impulsive traction.

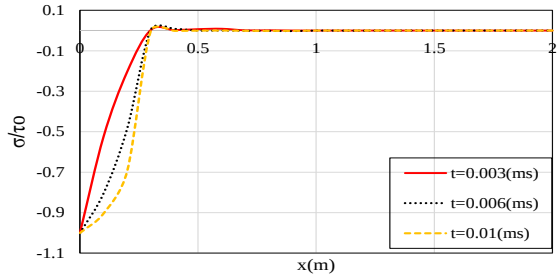

(a)

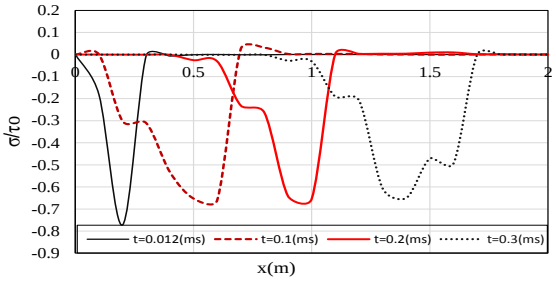

(b)

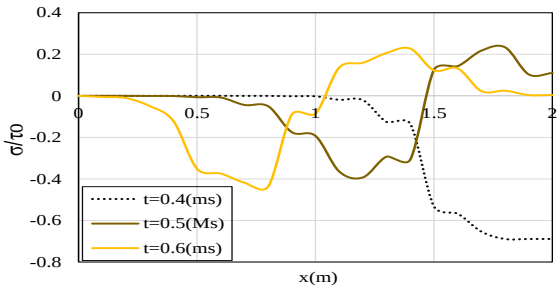

(c)

Fig.9
Propagation of the stress wave along the solid under mechanical shock, for various time instants.

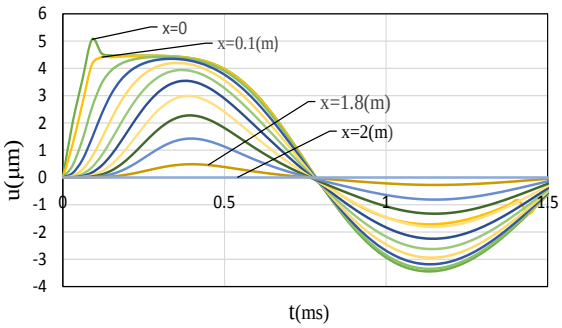

Fig.10
Displacement time history at different sections of the body under mechanical shock.

According to Fig. 11, at the beginning times, the initial points have the maximum displacement. By eliminating the applied stress, the displacement wave moves through the body over time. The propagation of the thermal wave may be traced in Fig. 12. As may be noted, the maximum of the temperature changes travels simultaneously with the maximum of the stress along the length (Fig.8).

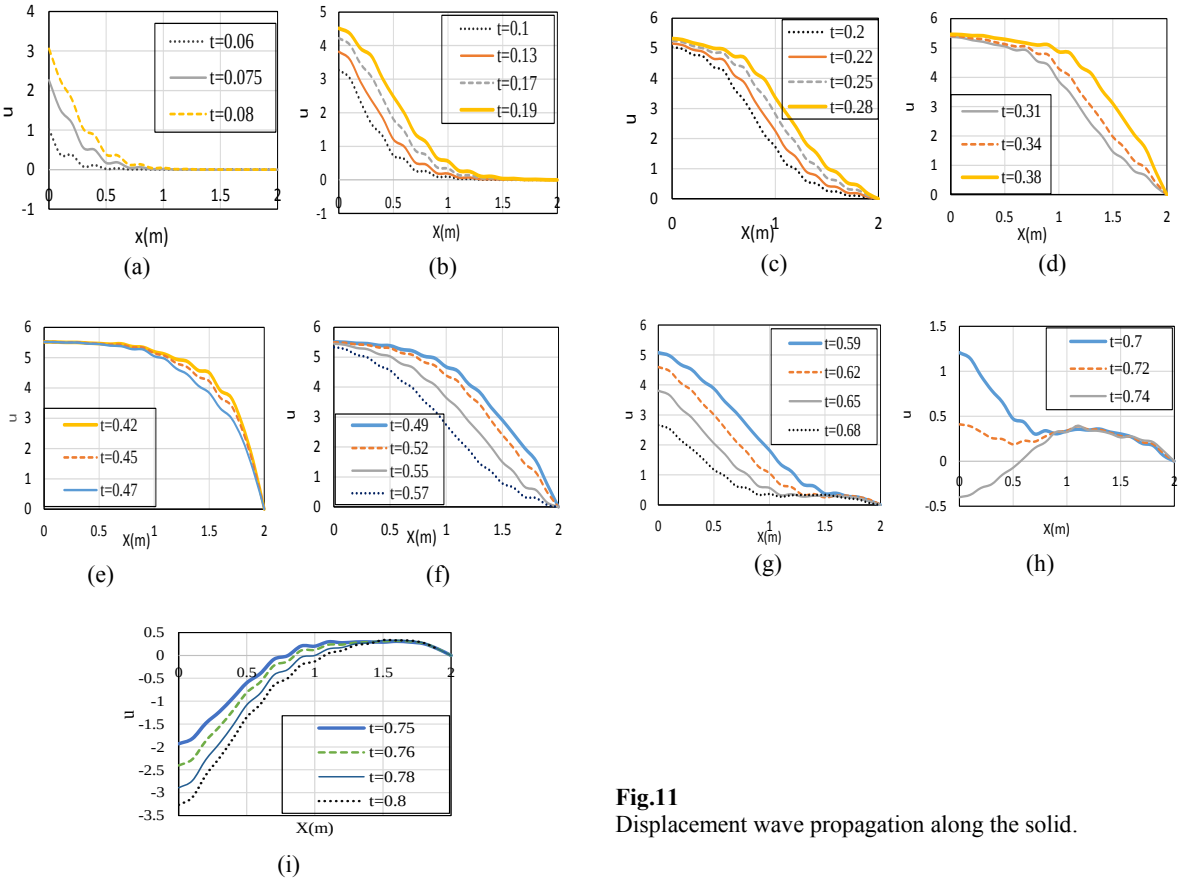

Fig.11
Displacement wave propagation along the solid.

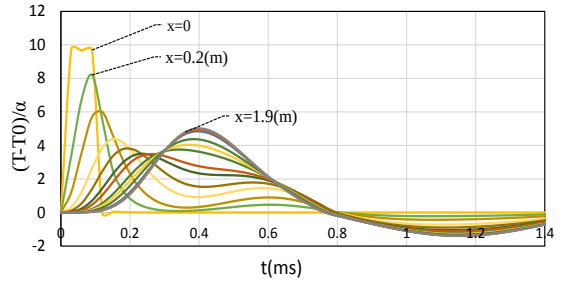

Fig.12
The time histories of the temperature-rise for different sections of the solid under mechanical shock.

It is clear that imposing compressive traction may lead to temperature rises whereas the tensile stresses induce a cooldown (negative temperature rises), as Fig. 12 confirms. For a more suitable imagination of the successive thermal propagations as well as reflection and finally, a complete mixing that eventually leads to a steady-state status, distributions of the temperature rise are plotted for very small to relatively large dimensionless time instants in Fig. 13. Recall that the end plane of the domain experiences a convection heat transfer and consequently, cooling. At $t \simeq 0.32(ms)$ the thermal wave reaches the end boundary (x=2m), for the first time. After that, the boundary temperature is rising. Then the wave manifests several-direction switching.

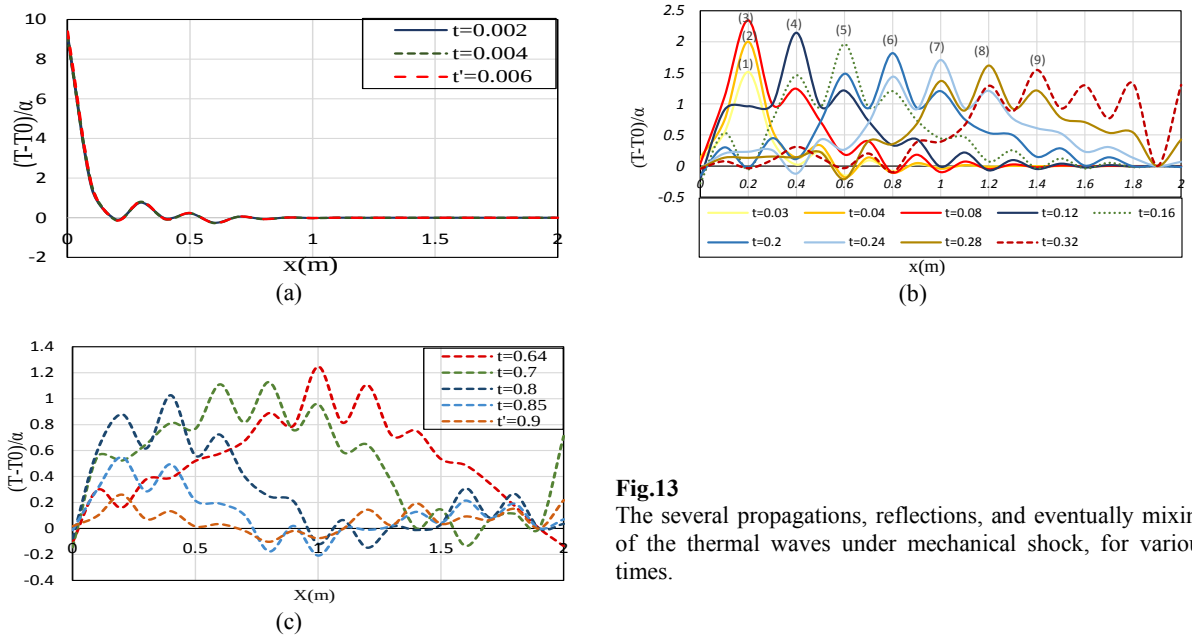

Fig.13
The several propagations, reflections, and eventually mixing of the thermal waves under mechanical shock, for various times.

5.2.2 Evaluation of the effects of the non-linear terms

Non-linearity of the governing equations adds significant complexity in the solution procedure and drastically increases the computational time. Therefore, it is necessary to check whether it affects the resulting accuracy of the results remarkably. In this regard, two cases are considered to compare the outcomes of the original non-linear formulation with those of the linearized one:

(i) The traction-type shock induces small strains whose order is in the practical range (e.g., of the order of 0.01),

(ii) The resulting strain is large (of the order of 0.1). This case is merely a sensitivity analysis; so that, it is postulated that the medium does not undergo plastic deformations.

In Figs. 14 and 15, respectively, effects of the non-linear parameters of the governing equations of motion and energy balance on distributions of the longitudinal displacement and stress can be investigated through comparing results of the non-linear and linearized formulations. The comparison has been made for cases when the wave moves toward the end of the solid. Although the strains are not large, the differences between the two types of results are noticeable.

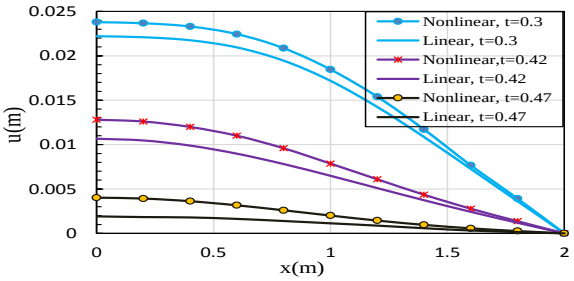

Fig.14
The differences between the longitudinal distributions of the displacements predicted by the full non-linear and the linearized formulations, for various time instants (small strains).

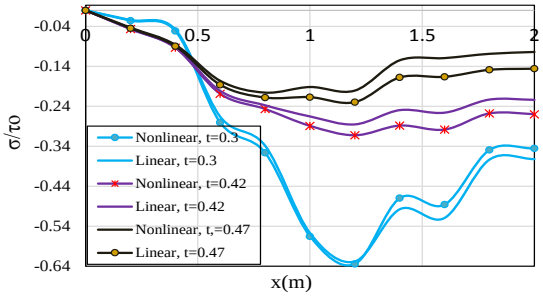

Fig.15
The differences between the longitudinal distributions of the stresses predicted by the full non-linear and the linearized formulations, for various time instants (small strains).

As mentioned before, the strains induced by the second type of traction shock are large enough. The time histories of the displacements and stresses observed at various planes of the medium are demonstrated in Figs. 16 and 17, respectively. Figs. 16 and 17 show that when the equations are linearized in cases where large deformations may happen, the displacement and stress components increase but the stress propagation speed decreases. It is obvious that increasing the flexibility of the solid generally leads to higher stresses and displacements [38]. Moreover, in non-linear systems, the natural frequencies and wave propagation speed are dependent on the magnitude of the external loads. For this reason, the propagation speed corresponding to the low tractions (the linearized formulation) is quite different from that of the large tractions (non-linear formulation). In other words, in non-linear analysis, no fixed speed of wave propagation can be defined.

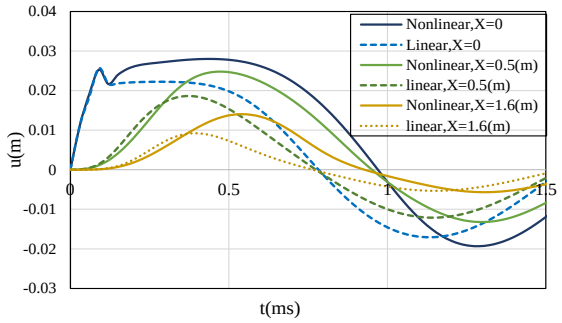

Fig.16
The differences between the time histories of the longitudinal displacements predicted for various sections by the full non-linear and the linearized formulations (large strains).

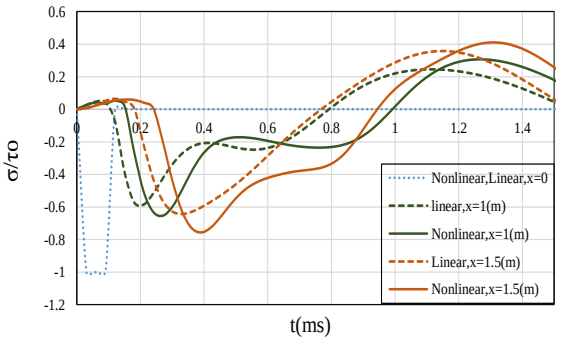

Fig.17
The differences between the time histories of the longitudinal stresses predicted for various sections by the full non-linear and the linearized formulations (large strains).

5.2.3 Anisotropic elastic solid exposed to a thermal and convection

Now, responses of the medium are investigated for the case where the front plane is under a sudden temperature rise while the back point is subjected to convection with the ambient [Eq. (16)]. Fig. 18 illustrates the time variation of temperature rise for three different sections of the medium. From Fig. 18 one may readily deduce that the maximum temperature rises occur before the thermal load removal and the heat convection mechanism has significantly suppressed the temperature rise for section far away from the front plane.

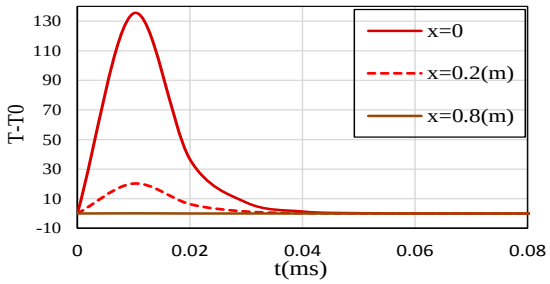

Fig.18
Temperature time history for different points of the solid under thermal shock.

Time histories of the longitudinal distribution of the temperature rise are illustrated in Fig. 19. Fig. 19(a) shows the temperature distribution during applying the thermal shock and the distributions after the shock removal are presented in Fig. 19(b). The longitudinal thermal wave propagation can easily be seen in this figure. As may be noted, the wave reaches the end plane of the body at $t = 0.38(ms)$, as before, which leads to the conclusion that the propagation velocity of the thermal shock is independent of the excitation type. This conclusion may be supported by Figs. 20 and 21 as well. Time variations of the displacement component are demonstrated in Fig. 20, for different sections of the medium. Furthermore, time variations of the longitudinal displacement distributions are shown in Fig. 20, for better imagination. This figure clearly illustrates the propagation of the displacement wave through the medium. Since the backplane of the domain is fixed, the thermal shock leads to movements in the negative direction of the x-direction (negative u'), as Fig. 21 shows. However, in the wave reflection period, the sign of this displacement changes.

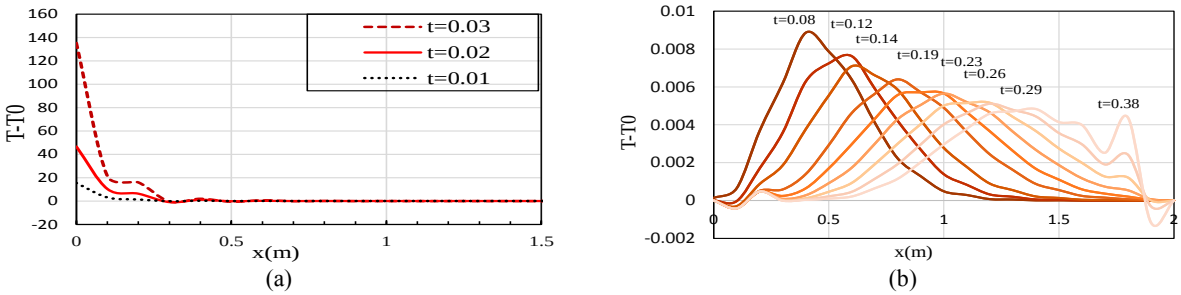

Fig.19
Distributions of the temperature-rise at various time instants, after the shock removal. The thermal wave propagation may readily be seen.

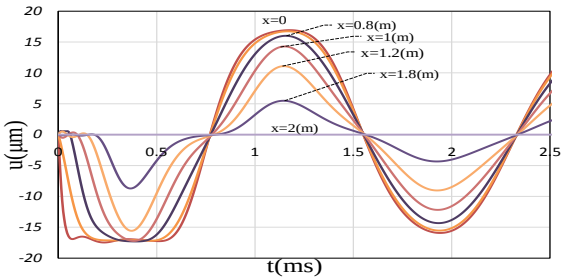

Fig.20
Time variations of the displacement wave, for various sections of the medium due to thermal shock.

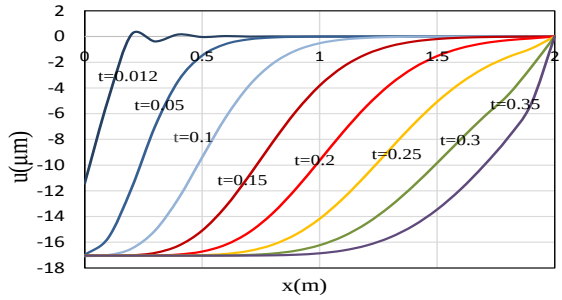

Fig.21
Propagation of the displacement wave in the medium due to thermal shock.

Fig. 22 demonstrates time variations of the stress at various sections of the body and the stress wave propagation. When the wave reaches the fixed end of the medium, its amplitude increases by a small amount, and a transition from the wave propagation to wave conversion, i.e., reflection begins. Since the thermal shock induces abrupt expansion at the early times of the wave propagation, the resulting stresses are tensile, at the earlier instants.

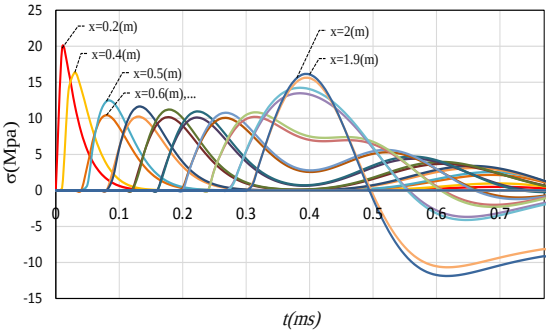

Fig.22
Propagation the stress wave at distinct sections of the medium due to thermal shock.

6 CONCLUSIONS

In this research, thermoelastic wave propagation, reflection, as well as the mixed phenomenon, are investigated. Some of the novelties of the present study can be presented as follow:

- Using the most general and nonlinear form of the strain tensor (Green's tensor) in terms of the displacement component. Furthermore, to account for the probability of large deformations, the second Piola-Kirchhoff stress tensor is employed.
- Nonlinear finite element terms are expanded according to new ideas of the weak formulation.
- An appropriate procedure for incorporation of the mechanical and thermal loading in the obtained finite element formulation is proposed, in conjunction with proposing an adequate algorithm for simultaneously treating the time-dependency and nonlinearity of final equations.
- Investigation of effects of the non-linear kinematic terms associated with the large deformations.

Some of the drawn practical conclusions are:

- The stress and thermal waves have interactions; compressive stress can lead to a temperature rise whereas tensile stress may lead to a local temperature decrease.
- The final temperature is the outcome of the combination of the consecutive thermal wave propagations and reflections.
- In contrast to traction, thermal shock induces tensile stresses in the medium at time instants immediately followed by the shock. Therefore, in contrast to the compressive traction, the thermal shock may assist the crack propagation mechanism. It is evident that in contrast to the theoretical results, the subsequent stress domains (e.g., those associated with the reflection period) are smaller, due to the structural damping.
- The terms associated with the large deformations show noticeable effects on the responses but do not alter the temperature rise, displacement, and stress distribution remarkably.
- Neglecting the non-linear terms leads to larger stresses and displacements and smaller speeds of wave propagation.
- In the non-linear analysis, no fixed speed of wave propagation can be defined.

REFERENCES

[1] Melan E., Parkus H., 1953, *Wärmespannungen in Platten*, Wärmespannungen, Springer.
[2] Nowacki W., 1970, Problems of thermoelasticity, *Progress in Aerospace Sciences* **10**: 1-63.
[3] Nowacki W., 1986, *Thermoelasticity*, Polish Scientific Publishers, Warsaw, and Pergamon Press, Oxford.
[4] Nowacki W., 1975, *Dynamic Problems of Thermoelasticity*, Springer Science & Business Media.
[5] Danilovskaya V.I., 1950, Thermal stresses in an elastic half-Space arising after a sudden heating of its boundary, *Pelageya Yakovlevna Kochina* **14**(3): 316-318.

[6] Manoach E., Ribeiro P., 2004, Coupled, thermoelastic, large amplitude vibrations of Timoshenko beams, *International Journal of Mechanical Sciences* **46**(11): 1589-1606.

[7] Vujošević L., Lubarda V., 2002, Finite-strain thermoelasticity based on multiplicative decomposition of deformation gradient, *Theoretical and Applied Mechanics* **28-29**: 379-399.

[8] Abo-El-Nour N., Ghaleb A., Maugin G., 1994, Harmonic wave generation in nonlinear thermoelasticity, *International Journal of Engineering Science* **32**(7): 1103-1116.

[9] Slemrod M., 1981, Global existence, uniqueness, and asymptotic stability of classical smooth solutions in one-dimensional non-linear thermoelasticity, *Archive for Rational Mechanics and Analysis* **76**(2): 97-133.

[10] Rawy E., Iskandar L., Ghaleb A., 1998, Numerical solution for a nonlinear, one-dimensional problem of thermoelasticity, *Journal of Computational and Applied Mathematics* **100**(1): 53-76.

[11] Sweilam N., 2007, Harmonic wave generation in non linear thermoelasticity by variational iteration method and Adomian's method, *Journal of Computational and Applied Mathematics* **207**(1): 64-72.

[12] Rogovoi A., Stolbova O., 2008, Evolutionary model of finite-strain thermoelasticity, *Journal of Applied Mechanics and Technical Physics* **49**(3): 500-509.

[13] Kocakaplan S., Tassoulas J.L., 2019, Wave propagation in initially-stressed elastic rods, *Journal of Sound and Vibration* **443**: 293-309

[14] Marzani A., Viola E., Bartoli I., Scalea F.L., Rizzo P., 2008, A semi-analytical finite element formulation for modeling stress wave propagation in axisymmetric damped waveguides, *Journal of Sound and Vibration* **318**: 488-505.

[15] Mirparizi M., Fotuhi A.R., Shariyat M., 2020, Nonlinear coupled thermoelastic analysis of thermal wave propagation in a functionally graded finite solid undergoing finite strain, *Journal of Thermal Analysis and Calorimetry* **139**: 2309-2320.

[16] Shariyat M., Khaghani M., Lavasani S.M.H., 2010, Nonlinear thermoelasticity, vibration, and stress wave propagation analyses of thick FGM cylinders with temperature-dependent material properties, *European Journal of Mechanics - A/Solids* **29**(3): 378-391.

[17] Shariyat M., 2009, A rapidly convergent nonlinear transfinite element procedure for transient thermoelastic analysis of temperature-dependent functionally graded cylinders, *Journal of Solid Mechanics* **1**(4):313-327.

[18] Shariyat M., 2012, Nonlinear transient stress and wave propagation analyses of the FGM thick cylinders, employing a unified generalized thermoelasticity theory, *International Journal of Mechanical Sciences* **65**(1):24-37.

[19] Parkus H., 1976, *Thermoelasticity*, Springer, New York.

[20] Eslami M.R., Hetnarski R.B., Ignaczak J., Noda N., Sumi N., Tanigawa Y., 2013, *Theory of Elasticity and Thermal Stresses*, Springer.

[21] Hetnarski R.B., Eslami M.R., 2009, *Thermal Stresses*, Springer.

[22] Eslami M.R., 2014, *Finite Elements Methods in Mechanics*, Springer International Publishing Switzerland.

[23] Shariyat M., Behzad H., Shaterzadeh A.R., 2018, 3D thermomechanical buckling analysis of perforated annular sector plates with multiaxial material heterogeneities based on curved B-spline elements, *Composite Structures* **188**: 89-103.

[24] Shariyat M., Niknami A., 2016. Impact analysis of strain-rate-dependent composite plates with SMA wires in thermal environments: Proposing refined coupled thermoelasticity, constitutive, and contact models, *Composite Structures* **136**: 191-203.

[25] Niknami A., Shariyat M., 2016, Refined constitutive, bridging, and contact laws for including effects of the impact-induced temperature rise in impact responses of composite plates with embedded SMA wires, *Thin-Walled Structures* **106**: 166-178.

[26] Shariyat M., Ghafourinam M., 2019, Hygrothermomechanical creep and stress redistribution analysis of thick-walled FGM spheres with temperature and moisture dependent material properties and inelastic radius changes, *International Journal of Pressure Vessels and Piping* **169**: 94-114.

[27] Shariyat M., Jahanshahi S., Rahimi H., 2019, Nonlinear Hermitian generalized hygrothermoelastic stress and wave propagation analyses of thick FGM spheres exhibiting temperature, moisture, and strain-rate material dependencies, *Composite Structures* **229**: 111364.

[28] Shariyat M., Ghaznavi A., Hosseini S.H., 2020, On inefficiency of the shape memory alloys in dynamically loaded sandwich plates with structural damping: New 3D zigzag-viscoelasticity theory and asymmetric transformations, *Thin–Walled Structures* **155**: 106879.

[29] Shariyat M., Lavasani S.M.H., Khaghani M., 2010, Nonlinear transient thermal stress and elastic wave propagation analyses of thick temperature-dependent FGM cylinders, using a second-order point-collocation method, *Applied Mathematical Modelling* **34**: 898-918.

[30] Youssef M., Lehaibi E., 2007, State-space approach of two-temperature generalized thermoelasticity, *International Journal of Solids and Structures* **44**(5): 1550-1562.

[31] Shariyat M., 2009, A nonlinear Hermitian transfinite element method for transient behavior analysis of hollow functionally graded cylinders with temperature-dependent materials under thermo-mechanical loads, *International Journal of Pressures Vessels and Piping* **86**: 280-289.

[32] Azadi M., Shariyat M., 2010, Nonlinear transient transfinite element thermal analysis of thick-walled FGM cylinders with temperature-dependent material properties, *Meccanica* **45**(3): 305-18.

[33] Alipour M.M., Shariyat M., 2018, Analytical layerwise stress and deformation analysis of laminated composite plates with arbitrary shapes of interfacial imperfections and discontinuous lateral deflections, *Composite Structures* **200**: 88-102.
[34] Shariyat M., Eslami M.R., 1996, Isoparametric finite-element thermoelasto-plastic creep analysis of shells of revolution, *International Journal of Pressures Vessels and Piping* **68**(3): 249-59.
[35] Ting E., Chen H., 1982, A unified numerical approach for thermal stress waves, *Computers & Structures* **15**(2): 165-175.
[36] Lee T.W., Sim W.J., 1992, Efficient time-domain finite element analysis for dynamic coupled thermoelasticity, *Computers & Structures* **45**(4): 785-93.
[37] Stailess Steel, Table of Technical Properties, Materials and Applications Series, 2007, http://www.euro-inox.org.
[38] Gould P.L., 1998, *Analysis of Shells and Plates*, Prentice Hall.